Supporting information

Tuning of electron transport layers using MXene/metal-oxide nanocomposites for perovskite solar cells and X-ray detectors

Sajjad Hussain[†1,2], Hailiang Liu[†3], Dhanasekaran Vikraman[4], Syed Hassan Abbas Jaffery[1,2], Ghazanfar Nazir[2], Faisal Shahzad[5], Khalid Mujasam Batoo[6], Jongwan Jung[1,2], Jungwon Kang[3*], Hyun-Seok Kim[4*]

[1]Hybrid Materials Center (HMC), Sejong University, Seoul 05006, Korea
[2]Department of Nanotechnology and Advanced Materials Engineering, Sejong University, Seoul 05006, Korea
[3]Convergence Semiconductor Research Center, Department of Electronics and Electrical Engineering, Dankook University, Yongin 16890, Korea
[4]Division of Electronics and Electrical Engineering, Dongguk University-Seoul, Seoul 04620, Korea
[5]Department of Metallurgy and Materials Engineering, Pakistan Institute of Engineering and Applied Sciences (PIEAS), Islamabad, Pakistan
[6]King Abdullah Institute for Nanotechnology, King Saud University, Riyadh-11451, Saudi Arabia

*Correspondence: hyunseokk@dongguk.edu (H-S.K); jkang@dankook.ac.kr (J.K.)
† These authors contributed equally.

S1 Synthesis of MXene

2D $Ti_3C_2T_x$-MXene was obtained by etching of Al layer from the commercially available MAX phase Ti_3AlC_2 using hydrogen fluoride (HF).[1] Concisely, commercial MAX phase was dispersed in a HF diluted solution (50%) and agitated slowly for 24 h at 60°C for the complete elimination of Al layers. The remnant solution was centrifuged and pounded with deionized (DI) water and absolute ethanol several times to separate residues until neutralize the pH. The final product was dehydrated under vacuum at 80 °C for 12 h.

S2 Synthesis of ZnO nanoparticles

Zinc acetate dihydrate ($Zn(O_2CCH_3)_2(H_2O)_2$) and sodium hydroxide (NaOH) were blended in the 25 mL of ethanol under the constant stirring and then placed on the hot plate at 80 °C for 5h. After the solution reached to room temperature slowly, the residues were separated and was with ethanol and de-ionized (DI) water multiple times using centrifugation. The final residues were annealed at 200^{o}C for 4 hours to form the ZnO powders

S3 Synthesis of Fe_3O_4 nanoparticles

Firstly, ferrous chloride ($FeCl_3 \cdot 6H_2O$) was dissolved in the 100 mL of DI water for 2h under the constant magnetic agitation. Next, sodium hydroxide (NaOH) was slowly mixed with the presence of nitrogen gas and solution bath was transferred on hot plate for 5 h at 80 °C. The final suspensions were washed multiple times with ethanol and DI water using centrifugation, dried at 200^{o}C vacuum oven.

S4 Characterization

The current density-voltage (J-V) measurements were evaluated in an electrometer (Keithley 6571B) and a solar simulator (San Ei Elec. XES 40S2-CE) using an AM 1.5G-filtered Xe lamp

exposure with an intensity of 100 mW/cm^2. The active area of the device is 4mm^2. External quantum efficiency (EQE) measurement was taken using Keithley (model 2400) with a monochromator (CS260-USB-1-MC-D) by ranging the wavelength from 300 to 800 nm. the suggested detector was combined with CsI (Tl) scintillators (Hamamatsu J13113) to convert incident X-ray photons into visible photons and the produced charge carriers during exposure were measured with the electrometer. The scintillator-coupled detector J-V characteristics were verified using an X-ray generator (AJEX 2000H). The distance between the X-ray source and the scintillator-coupled detector was approximately 30 cm, and the exposure X-ray dose was measured using an ion chamber (Capintec CII50) at the same distance. The operating conditions of X-ray generator were fixed at 1.57 sec, 80 kVp and 63 mAÂus for X-ray exposure time, tube voltage and tube current, respectively for all the experiments. The constant 3.34 mGy of dose rate and -0.6 V of applied bias voltage for X-ray source were used for the all the measurement. To tune the charge-carrier collection, the bias voltage to the detector from -0.2 to -1.0V and dose rate from 1.19 to 5.56 mGy were applied. The CCD during X-ray exposure and sensitivity were computed from the measured charge amount. The sensitivity, related to X-ray photon-to-charge conversion efficiency, was calculated using the following equation.

$$Sensitivity\ (^{mA}/_{Gy \cdot cm^2}) = \frac{Charges\ during\ the\ X-ray\ ON[mA] -\ Charges\ during\ the\ X-ray\ OFF\ [mA]}{Absorbed\ dose\ [Gy] \cdot Detection\ Area\ [cm^2]}$$

The absorbed doses from the exposure was measured using the ion chamber.

The electronic structure of ZnO, Fe_3O_4, MXene, MXene/ZnO or MXene/Fe_3O_4 were examined by Raman spectroscope (Renishaw inVia RE04). X-ray diffraction measurements were achieved by a Rigaku D/max-2500 diffractometer with Cu-K_α radiation as the X-ray source. Energy dispersive by X-ray combined JEOL JSM-6700F FESEM was utilized to analyze the surface morphology of the nanostructures. Atomic force microscopy (Park Systems XE-150) was

conducted to measure the roughness in non-contact mode with 10 μm × 10 μm scan size. The atomic structure of MXene/ZnO or MXene/Fe_3O_4 was characterized by transmission electron microscope (JEOL-2010F TEM) with 200k eV accelerating voltage. Gatan Digital Micrograph software (version - 3.21) was used to process the TEM images. X-ray photoelectron spectroscopy analysis was performed using PHI 5000 Versa Probe equipped with a monochromatic Al Kα radiation source (25W, 6.7×10^{-8} Pa). UV-vis optical spectroscopy (Optizen 2120UV) was used to measure the absorption spectra of HTLs. Theta Probe (Thermo) X-ray photoelectron spectrometer was used to measure ultraviolet photoelectron spectra using He1 (21.2 eV) source with a step size of 0.05 eV.

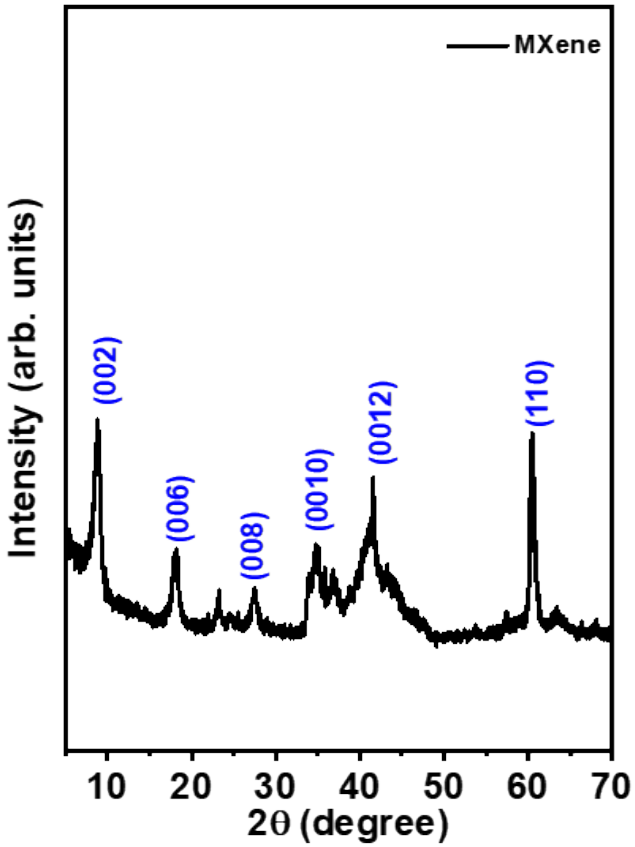

Figure S1. XRD pattern of $Ti_3C_2T_x$ MXene sheets.

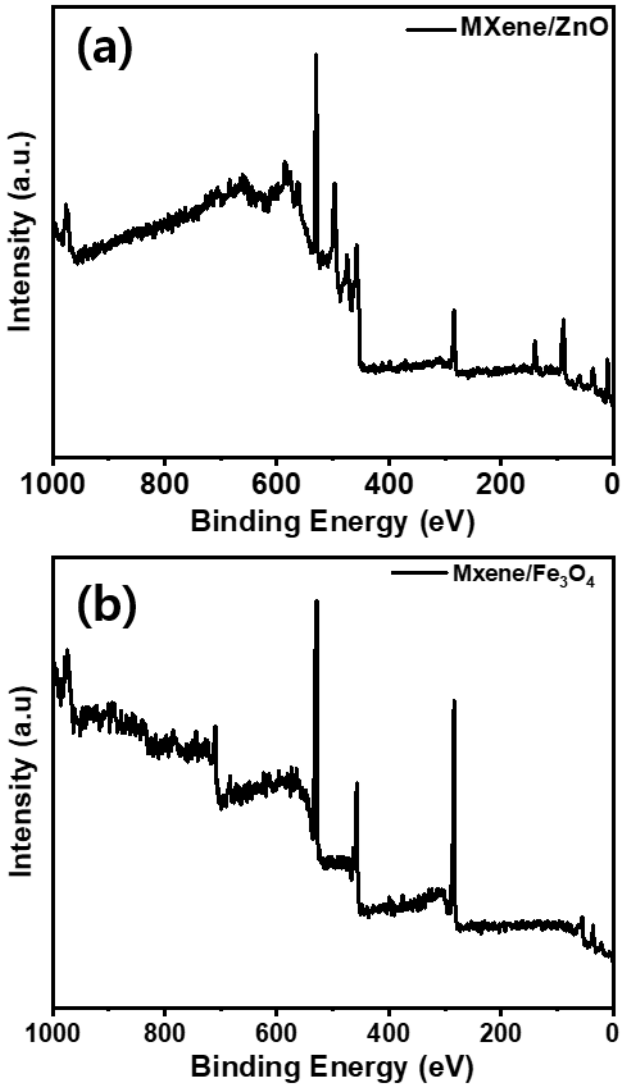

Figure S2. XPS survey spectrum: (a) MXene/ZnO and (b) MXene/Fe_3O_4.

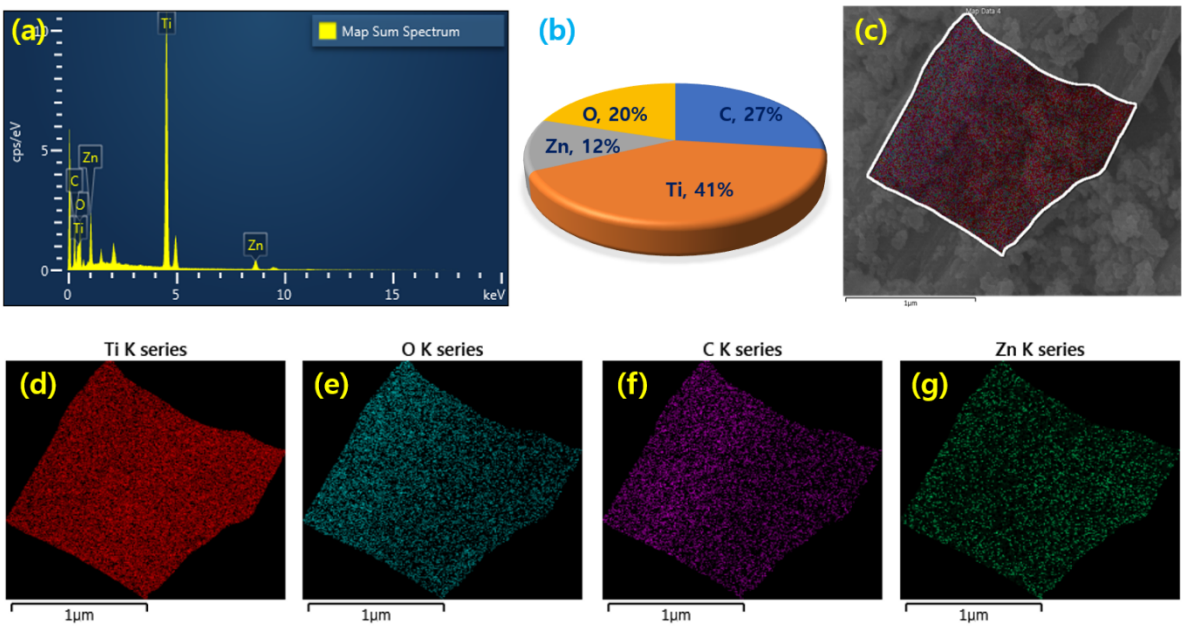

Figure S3. MXene/ZnO nanocomposites: (a) EDS-FESEM image and (b) composition; (c) elemental mapping and their elements distribution (d) Ti, (e) O, (f) C and (g) Zn atoms.

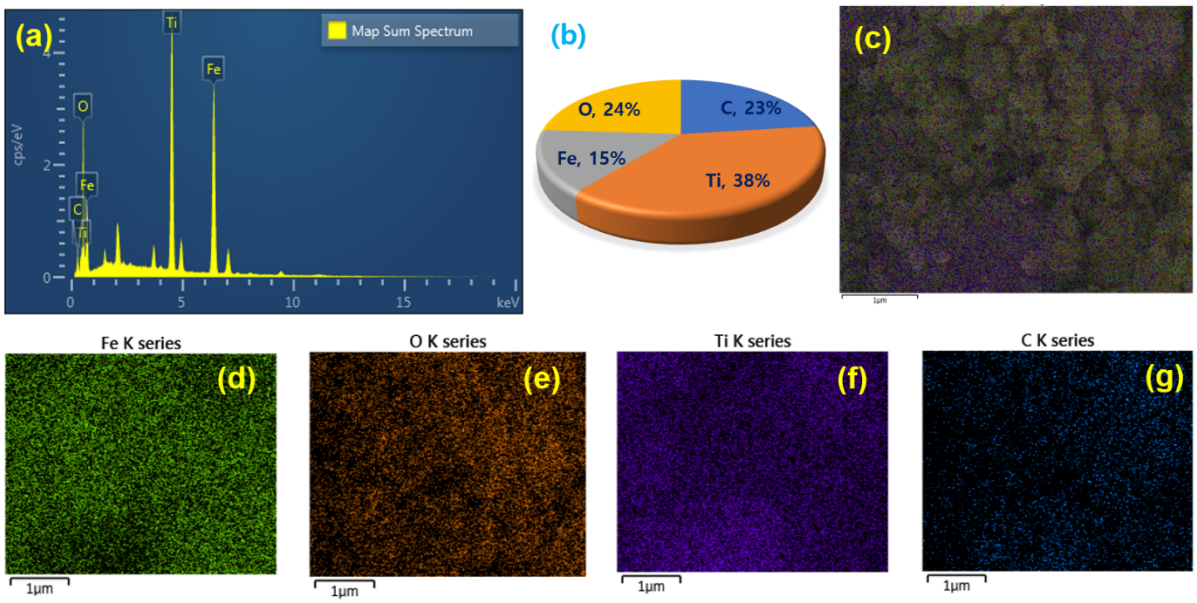

Figure S4. MXene/Fe_3O_4 nanocomposites: (a) EDS-FESEM image and (b) composition; (c) elemental mapping and their elements distribution (d) Fe, (e) O, (f) Ti and (g) C atoms.

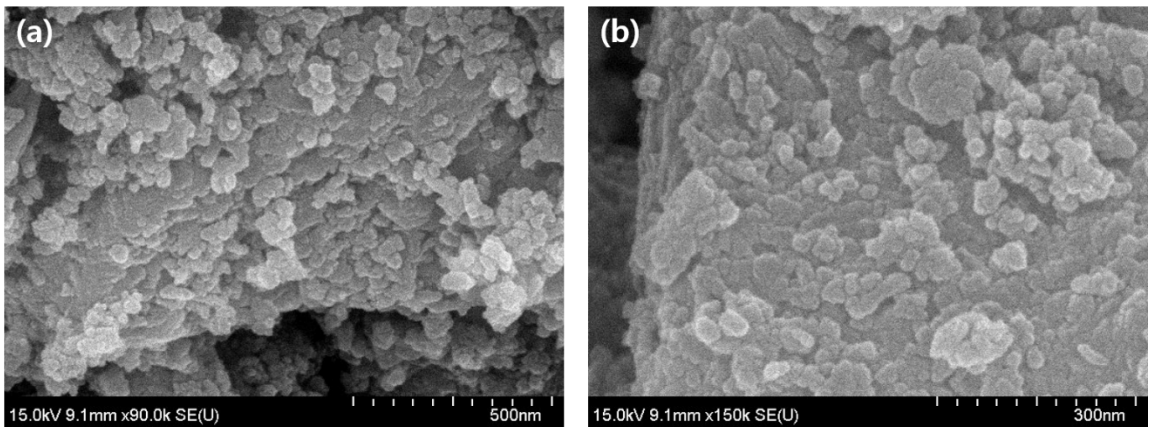

Figure S5. FESEM images of Fe_3O_4 nanoparticles.

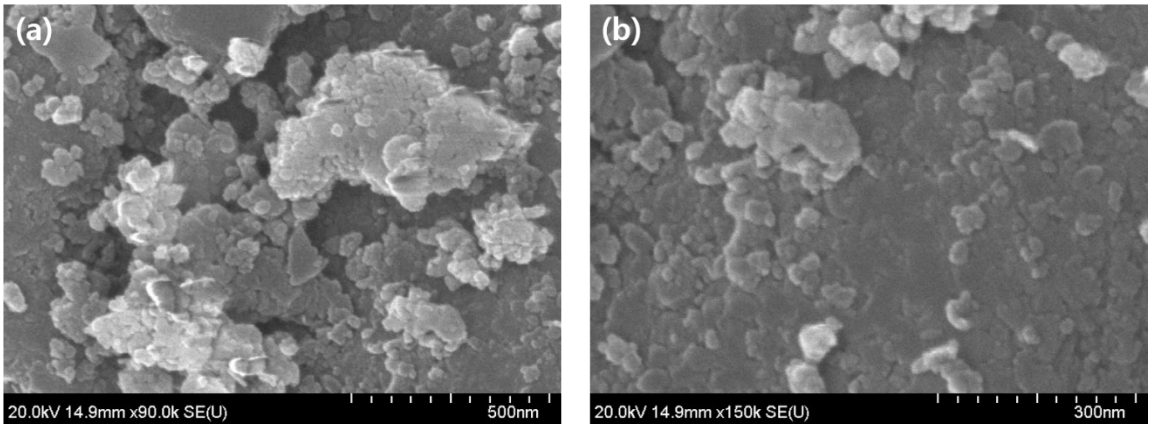

Figure S6. FESEM images of ZnO nanoparticles.

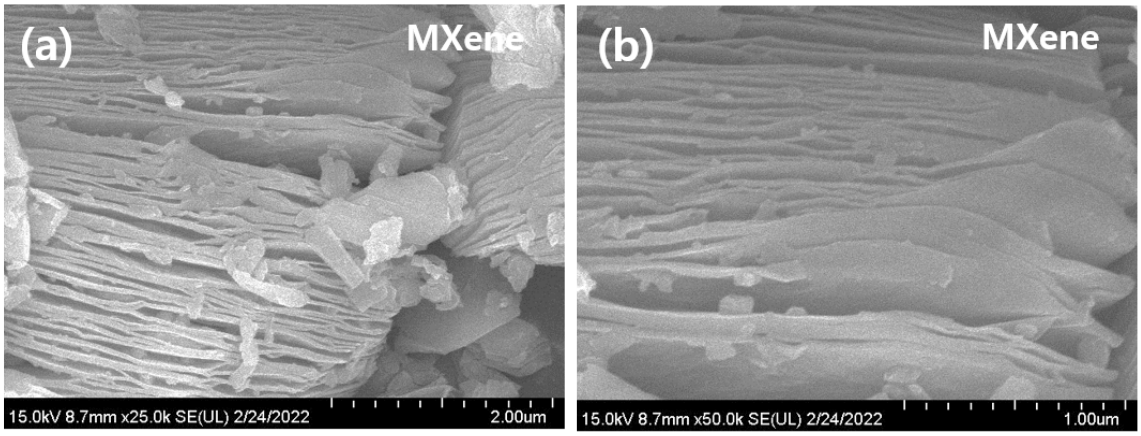

Figure S7. FESEM images of MXene nanoparticles.

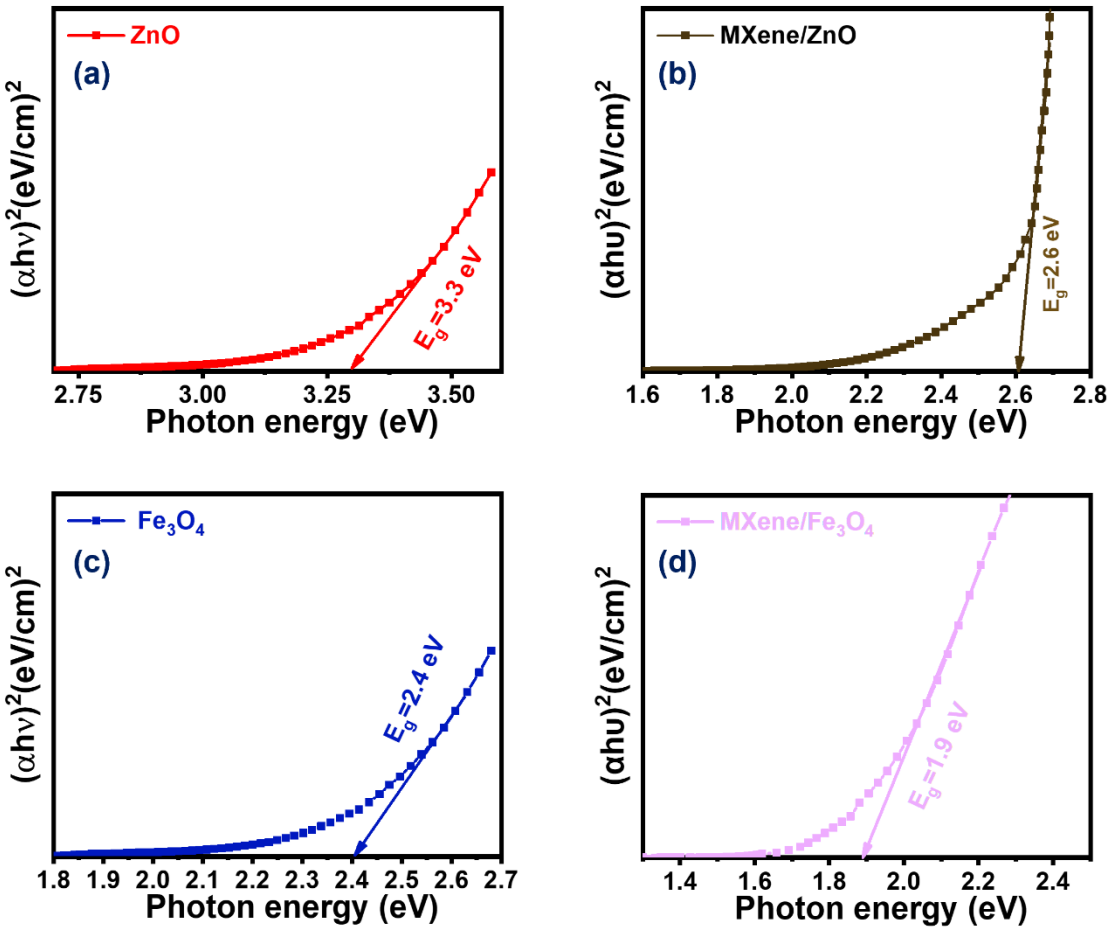

Figure S8. Optical band gap plot of prepared (a) ZnO and (b) Fe_3O_4 nanoparticles

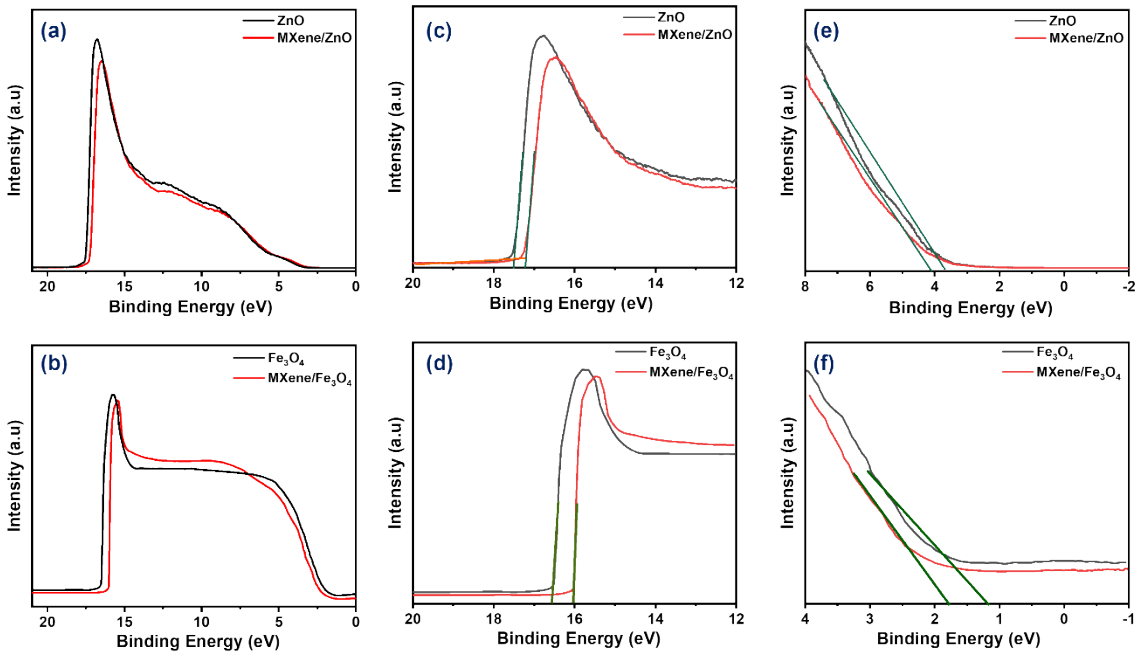

Figure S9. UPS profiles for the prepared (a) ZnO and (b) Fe_3O_4 based nanostructures, $E_{cut\text{-}off}$ region for the (c) ZnO and (d) Fe_3O_4 based nanostructures and Fermi (E_F) level positions of (e) ZnO and (f) Fe_3O_4 based nanostructures.

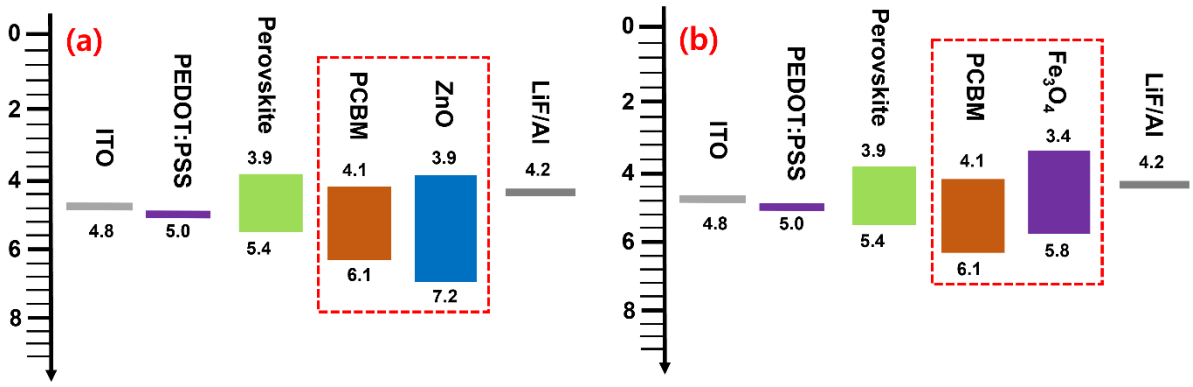

Figure S10. Energy level of (a) ITO/PEDOT:PSS/$Cs_{0.1}MA_{0.9}PbI_3$/ZnO@PCBM/LiF/Al and (b) ITO/PEDOT:PSS/$Cs_{0.1}MA_{0.9}PbI_3$/Fe_3O_4@PCBM/LiF/Al.

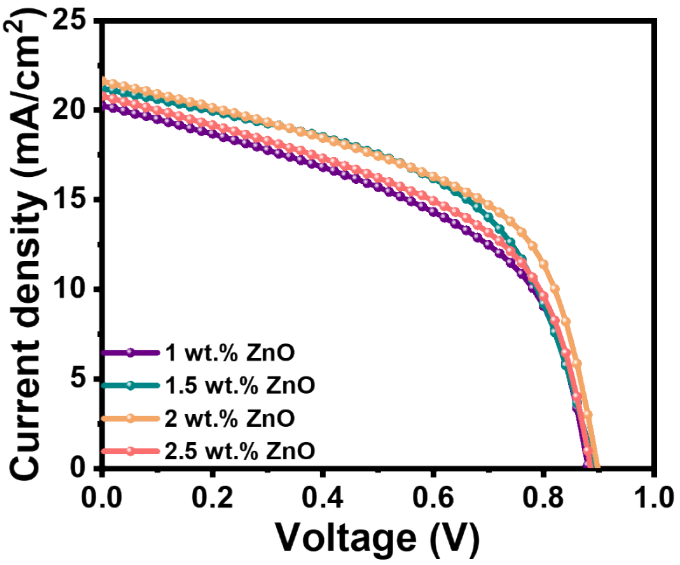

Figure S11. J−V curves of perovskite solar cells using different concentration of ZnO with different concentration (1, 1.5, 2 and 2.5 wt%) blended with PCBM ETL.

Table S1. Photovoltaic performances of prepared perovskite devices with different concentrations of ZnO nanoparticles blended ETL.

ZnO@PCBM	**V_{OC} [V]**	**J_{SC} [mA/cm^2]**	**FF [%]**	**PCE [%]**	**R_S [Ω·cm^2]**
1 wt.%	0.881	20.247	57.79	10.31	172.16
1.5 wt.%	0.891	21.198	59.45	11.23	163.41
2 wt.%	0.897	21.623	60.16	11.67	158.42
2.5 wt.%	0.884	20.793	59.20	10.88	167.23

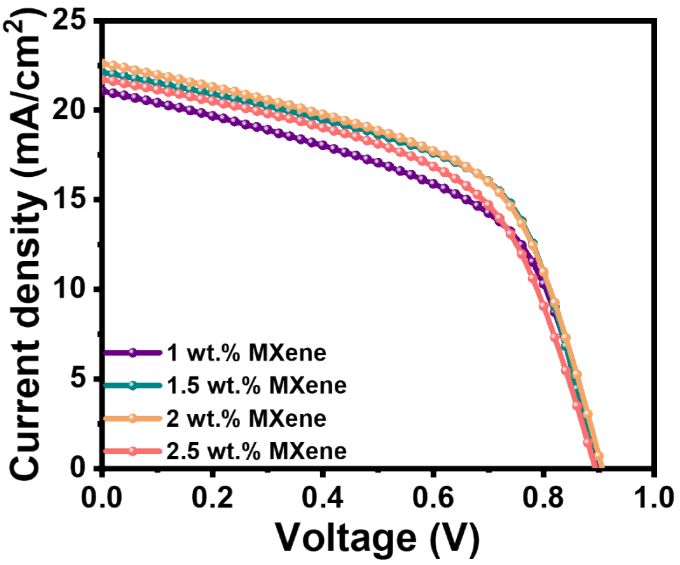

Figure S12. J−V curves of perovskite solar cells using different concentration of MXene with different concentration (1, 1.5, 2 and 2.5 wt%) blended with PCBM ETL.

Table S2. Photovoltaic performances of prepared perovskite devices with different concentrations of MXene blended ETL.

MXene@PCBM	**V_{OC} [V]**	**J_{SC} [mA/cm^2]**	**FF [%]**	**PCE [%]**	**R_S [Ω·cm^2]**
1 wt.%	0.895	21.076	59.42	11.21	164.87
1.5 wt.%	0.893	22.114	61.37	12.12	151.36
2 wt.%	0.905	22.598	62.78	12.84	143.18
2.5 wt.%	0.893	21.698	60.53	11.73	157.23

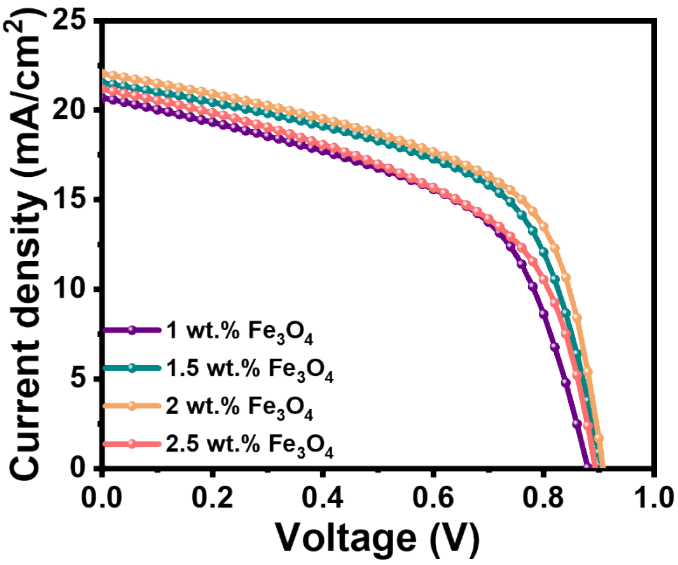

Figure S13. J−V curves of perovskite solar cells using different concentration of Fe_3O_4 with different concentration (1, 1.5, 2 and 2.5 wt%) blended with PCBM ETL.

Table S3. Photovoltaic performances of prepared perovskite devices with different concentrations of Fe_3O_4 blended ETL.

Fe_3O_4@PCBM	**V_{OC} [V]**	**J_{SC} [mA/cm^2]**	**FF [%]**	**PCE [%]**	**R_S [Ω·cm^2]**
1 wt.%	0.880	20.685	59.38	10.81	168.24
1.5 wt.%	0.905	21.529	60.46	11.78	157.43
2 wt.%	0.907	22.037	61.18	12.23	150.17
2.5 wt.%	0.893	21.186	59.23	11.26	164.91

Table S4. Photovoltaic performances of prepared perovskite devices using MXene/Fe_3O_4 hybrid nanoparticles as ETL.

Device	V_{OC} [V]	J_{SC} [mA/cm^2]	FF [%]	PCE [%]	R_S [Ω·cm^2]
1 wt.%	0.901	22.187	61.22	12.24	149.16
1.5 wt.%	0.906	22.945	63.73	13.25	139.24
2 wt.%	0.902	23.421	65.27	13.79	132.65
2.5 wt.%	0.906	22.478	62.65	12.76	145.38

Table S5. Photovoltaic performances of prepared perovskite devices with different concentrations of MXene/ZnO hybrid nanoparticles blended ETL.

MXene/ZnO@PCBM	V_{OC} [V]	J_{SC} [mA/cm^2]	FF [%]	PCE [%]	R_S [Ω·cm^2]
1 wt.%	0.884	21.389	62.72	11.86	156.34
1.5 wt.%	0.908	22.416	62.98	12.82	143.29
2 wt.%	0.904	22.987	64.05	13.31	138.76
2.5 wt.%	0.900	21.932	62.51	12.34	149.58

Table S6. Comparison of photovoltaic parameters with different materials doping ETL

Sample	PCE (%)	Reference	Improvement (%)
Pure PCBM (ETL)	8.15	[7]	
ETL doping with DMBI	12.53		53.74
Pure PCBM (ETL)	10.05	[8]	
ETL doping with oleamide	12.69		26.26
Pure PCBM (ETL)	10.8	[9]	
ETL doping with graphdiyne	13.9		28.70
Pure PCBM (ETL)	11.22	[10]	
ETL doping with CdSe quantum dot	13.73		22.37
Pure PCBM (ETL)	11.27	[11]	
ETL doping with graphene oxide	12.82		13.75
Pure PCBM (ETL)	11.43	[12]	
ETL doping with CoSe	14.91		30.44
Pure PCBM (ETL)	12.1	[13]	
ETL doping with carbon nanodots	13.4		10.74
Pure PCBM (ETL)	12.79	[14]	
ETL doping with GQDs	16.41		28.30
Pure PCBM (ETL)	12.72	[15]	11.39
ETL doping with ZnO	14.17		
Pure PCBM (ETL)	7.6	[16]	86.84
ETL doping with α-Fe_2O_3	14.2		
Pure PCBM (ETL)	15.16	[17]	18.40
ETL doping with MXene	17.95		
Pure PCBM (ETL)	10.58	This work	
ETL doping with MXene/Fe_3O_4	13.79		30.34
ETL doping with MXene/ZnO	13.31		25.80

Table S7. X-ray detector performance for different concentrations of MXene nanoparticles blended in ETL.

ETL	CCD-DCD [μA/cm^2]	Sensitivity [mA/Gy•cm^2]
MXene -1%	11.42	3.42
MXene -1.5%	12.66	3.79
MXene -2 %	13.89	4.16
MXene -2.5	12.22	3.66

Table S8. X-ray detector performance for different concentrations of ZnO blended in ETL.

ETL	CCD-DCD [μA/cm^2]	Sensitivity [mA/Gy•cm^2]
ZnO -1%	9.92	2.97
ZnO -1.5%	11.56	3.46
ZnO -2 %	12.16	3.64
ZnO -2.5	10.72	3.21

Table S9. X-ray detector performance for different concentrations of Fe_3O_4 blended in ETL.

ETL	CCD-DCD [μA/cm^2]	Sensitivity [mA/Gy•cm^2]
Fe_3O_4 -1%	10.59	3.17
Fe_3O_4 -1.5%	12.32	3.69
Fe_3O_4 -2 %	12.93	3.87
Fe_3O_4-2.5	11.62	3.48

Table S10. X-ray detector performance for different concentrations of MXene/ZnO blended in ETL.

ETL	CCD-DCD [μA/cm^2]	Sensitivity [mA/Gy•cm^2]
MXene/ZnO -1%	12.32	3.69
MXene/ZnO -1.5%	13.83	4.14
MXene/ZnO -2 %	14.73	4.41
MXene/ZnO -2.5	13.09	3.92

Table S11. X-ray detector performance for different concentrations of MXene/Fe_3O_4 blended in ETL.

ETL	CCD-DCD [μA/cm^2]	Sensitivity [mA/Gy•cm^2]
MXene/Fe_3O_4 -1%	12.86	3.85
MXene/Fe_3O_4 -1.5%	14.63	4.38
MXene/Fe_3O_4 -2 %	15.46	4.63
MXene/Fe_3O_4-2.5	13.73	4.11

References

1. S. Hussain, D. Vikraman, M. T. Mehran, M. Hussain, G. Nazir, S. A. Patil, H.-S. Kim and J. Jung, *Renewable Energy*, 2022, **185**, 585-597.
2. D. Vikraman, H. J. Park, S.-I. Kim and M. Thaiyan, *Journal of Alloys and Compounds*, 2016, **686**, 616-627.
3. V. Dhanasekaran, T. Mahalingam, R. Chandramohan, J. K. Rhee and J. P. Chu, *Thin Solid Films*, 2012, **520**, 6608-6613.
4. J. Lin, Y. Yu, Z. Zhang, F. Gao, S. Liu, W. Wang and G. Li, *Advanced Functional Materials*, 2020, **30**, 1910479.
5. M. R. Habib, H. Li, Y. Kong, T. Liang, S. M. Obaidulla, S. Xie, S. Wang, X. Ma, H. Su and M. Xu, *Nanoscale*, 2018, **10**, 16107-16115.

6. A. Y. Kobitski, R. Scholz, D. R. T. Zahn and H. P. Wagner, *Physical Review B*, 2003, **68**, 155201.
7. J.-H. Bae, Y.-J. Noh, M. Kang, D.-Y. Kim, H.-B. Kim, S.-H. Oh, J.-M. Yun and S.-I. Na, *RSC advances*, 2016, **6**, 64962-64966.
8. F. Xia, Q. Wu, P. Zhou, Y. Li, X. Chen, Q. Liu, J. Zhu, S. Dai, Y. Lu and S. Yang, *ACS Applied Materials & Interfaces*, 2015, **7**, 13659-13665.
9. C. Kuang, G. Tang, T. Jiu, H. Yang, H. Liu, B. Li, W. Luo, X. Li, W. Zhang and F. Lu, *Nano letters*, 2015, **15**, 2756-2762.
10. X. Zeng, T. Zhou, C. Leng, Z. Zang, M. Wang, W. Hu, X. Tang, S. Lu, L. Fang and M. Zhou, *Journal of Materials Chemistry A*, 2017, **5**, 17499-17505.
11. G. Kakavelakis, T. Maksudov, D. Konios, I. Paradisanos, G. Kioseoglou, E. Stratakis and E. Kymakis, *Advanced Energy Materials*, 2017, **7**, 1602120.
12. S. Chen, S. Yang, H. Sun, L. Zhang, J. Peng, Z. Liang and Z.-S. Wang, *Journal of Power Sources*, 2017, **353**, 123-130.
13. R. Subair, D. Di Girolamo, M. Bodik, V. Nadazdy, B. Li, P. Nadazdy, Z. Markovic, M. Benkovicova, J. Chlpik and M. Kotlar, *Solar Energy*, 2019, **189**, 426-434.
14. D. H. Shin, J. M. Kim, S. H. Shin and S.-H. Choi, *Dyes and Pigments*, 2019, **170**, 107630.
15. S. Park, W. Jang and D. H. Wang, *Macromolecular Research*, 2018, **26**, 472-476.
16. Q. Hou, J. Ren, H. Chen, P. Yang, Q. Shao, M. Zhao, X. Zhao, H. He, N. Wang and Q. Luo, *ChemElectroChem*, 2018, **5**, 726-731.
17. V. S. Chava, P. Chandrasekhar, A. Gomez, L. Echegoyen and S. T. Sreenivasan, *ACS Applied Energy Materials*, 2021, **4**, 12137-12148.